Journal of Marine Science and Technology

Volume 29 | Issue 6 Article 2

Simulation of a Ship and Tension Leg Platform Wind Turbine Collision

Jiamin Guo
Shanghai Maritime University, Shanghai, China, jmguo@shmtu.edu.cn

Yu Zhao
Shanghai Maritime University, Shanghai, China

Weigang Chen
Zhejiang Southest Space Frame Co., LTD, Hangzhou, China

Guangeng Zhou
Zhejiang Southest Space Frame Co., LTD, Hangzhou, China

Recommended Citation
Guo, Jiamin; Zhao, Yu; Chen, Weigang; and Zhou, Guangeng (2022) "Simulation of a Ship and Tension Leg Platform Wind Turbine Collision," *Journal of Marine Science and Technology*: Vol. 29: Iss. 6, Article 2.
DOI: 10.51400/2709-6998.2553
Available at: https://jmstt.ntou.edu.tw/journal/vol29/iss6/2

RESEARCH ARTICLE

Simulation of a Ship and Tension Leg Platform Wind Turbine Collision

Jiamin Guo [a,*], Yu Zhao [a], Weigang Chen [b], Guangeng Zhou [b]

[a] School of Ocean Science and Engineering, Shanghai Maritime University, Shanghai 200135, China
[b] Zhejiang Southest Space Frame Co., LTD, Hangzhou 311209, China

Abstract

Collisions between ships and tension leg platform wind turbines (TLPWTs) result in the TLPWT damage, including tower damage and tension leg breakage. This paper details a collision between a ship and TLPWT simulated using the LS-DYNA software package. During simulation, the behaviors of the water around the ship and of the TLPWT were processed using the constant added mass and the fluid−structure interaction methods, respectively. The results indicate that the energy conversion during collision is generally consistent with the law of conversion of energy, suggesting that the simulation's calculations are acceptable. The TLPWT simulation results imply that two distinct collisions occurred during the broader collision period because of TLPWT pitch or roll, and the simulated damage mainly occurred in the contact areas. All tension legs were not slack during collision because of prestress, and the responses of the symmetrical tension legs were largely equivalent. The response of the TLPWT decreased over time due to water resistance. The results of this paper can be consulted to prevent and reduce losses caused by ship−TLPWT collisions.

Keywords: Tension leg platform wind turbine, Collision, Fluid−structure interaction, LS-DYNA

1. Introduction

Wind energy development takes place onshore, offshore, and finally, in deep sea areas. Particular research focus has been given to offshore wind turbines (OWTs) [1]. Several types of OWT are now produced. The monopile foundation wind turbine is the simplest wind turbine [2] and is widely used in offshore areas. With the further development of deep-sea wind energy, the floating foundation, which is more suitable for deep sea use, has also emerged. The main types of floating foundations are spar [3], semisubmersible [4] and tension leg platform (TLP) foundations [5]. TLP wind turbines (TLPWT) are still under development. Research on TLPs has been widely conducted. Bachynski et al. [6] compared five types of TLPWTs and studied the influence of their different parameters. Nematbakhsh [7] simulated TLPWTs and noted that these tension legs might be relaxed under maximal wave height. Heather et al. [8] proposed a small-scale test model for floating wind turbines and verified the model's reliability at laboratory conditions. Andrew et al. [9] proposed a unified TLPWT model that accounts for the effects of both wind waves and damping. In recent years, the possibility of collisions between ships and floating wind turbines has increased due to the growing numbers of OWTs and the expansion of sea routes. Collisions between marine structures can have severe consequences. Extensive research on ship−ship, ship−bridge, and ship−offshore platform collisions has been conducted. Aditya et al. [10] studied the rebounding phenomenon of a striking ship and its effect on the crashworthiness of the impacted ship structure under the configurations of predefined scenarios. Sha et al. [11] used numerical simulation methods to analyze the safety of a

Received 28 October 2020; revised 18 January 2021; accepted 27 July 2021.
Available online 27 December 2021

* Corresponding author.
E-mail address: jmguo@shmtu.edu.cn (J. Guo).

https://doi.org/10.514/2709-6998.2553

pontoon under the impact load of a ship and studied the pontoon's dynamic response. Travanca et al. [12] conducted a series of finite element analyses to provide a clearer understanding of the strain energy dissipation phenomenon, especially in terms of ship−offshore structure interactions during collisions. Minorsky [13] classified the collision problem into independent mechanisms of structural damage and kinetic energy loss, which are internal and external mechanisms, respectively. The kinetic energy loss problem is solved using completely inelastic collision theory, and the influence of the fluid on the collision is simplified by applying the additional quality method. In postcollision studies, many scholars have improved Minorsky's empirical formula. Among them, Paik [14] expanded the scope of Minorsky's formula. Aditya et al. [15] studied ship−ship collisions with different ship types; In their study, they analyzed postcollision structural damage and energy conversion before and after a collision. Moulas et al. [16] developed a numerical nonlinear finite element analysis approach to evaluate the damage to wind turbine foundations from a collision with an offshore support vessel. Gjerde et al. [17] studied the mechanism of a collision between a ship and jacket platform; They analyzed the classification of collision degree and the failure mechanism of platform components. Ou and Ren [18] simulated a collision between a ship and a fixed single-pile foundation, and they analyzed the stress change, plastic strain, and collision force upon the single-pile foundation. Hamann et al. [19] simulated a collision between a 200,000-Mg tanker and a gravity foundation. Hao et al. [20] indicated that the jacket foundation achieved optimum comprehensive anti-impact performance under low-energy collisions by generating the minimum collision force among three foundation types (monopile, tripod, and jacket). Bela et al. [21] performed simulations of nonlinear collisions between a rigid striking ship and an OWT. Mo et al. [22] performed transient response and damage analysis on the grouted connections of monopile OWTs when subjected to ship collision impact. Ren et al. [23] proposed an anti-collision device for single-pile OWTs to reduce pile foundation damage. Until now, only limited research has been conducted on TLPWT collisions because they were developed much later than offshore oil platforms. If the tension legs fracture after collision, the OWT will be irreparably damaged. Thus, studying the collision between TLPWTs and ships is of critical concern.

The layout of the paper is as follows: section 2 provides the basic theory for the effects of surrounding water, section 3 gives the detailed model for the collision simulation, section 4 relates the results obtained from the collision simulation, which suggest that it is reasonable to simulate the effect of water on the TLPWT and the ship using fluid−structure interaction (FSI) and constant added mass (CAM) methods, respectively.

2. Theory on surrounding water effects

Collision analysis encompasses examining external dynamics and internal mechanics. The water surrounding objects has effect on collisions. Thus, analyzing the effects of surrounding water is a key step in collision analysis. The effects of surrounding water are considered using two methods: the CAM method and the FSI method. The FSI method has higher accuracy in simulating the effects of surrounding water than the CAM method [24,25]; however, it also requires a more complicated model and longer calculation time. The theories behind these two methods are summarized in the following subsections.

2.1. FSI method

The FSI method can provide a solution to a fully coupled ship collision problem in which the surrounding water flow is explicitly simulated and actual ship motion is considered when the contact force is being evaluated. The solution is obtained using numerical methods such as computational fluid dynamics, arbitrary Lagrange−Euler (ALE) methods, smoothing particle hydrodynamics, and other simplified fluid dynamic simulation methods [25]. Currently, the ALE method is widely used in marine structure collision analyses. The ALE method is convenient for designers to implement because this formulation is included in most design or finite element software (e.g., Fluent, LS-DYNA) platforms. The LS-DYNA program provides a various materials (such as water and air) and Euler substances for achieving coupling between a fluid and the solid structure by using the ALE algorithm. However, the ALE solver in LS-DYNA is not a complete Navier−Stokes solver; it does not consider fluid boundary layers. The effect of fluid viscosity is only derived from the material model [26]. The fully coupled ALE method requires considerable modeling work and computing resources. The solve was implemented using the Lagrangian−Eulerian method in LS-DYNA. Because a TLPWT was the key research object in this paper, the FSI between water and TLPWT was simulated based on the FSI method.

2.2. CAM method

Minorsky [27] first proposed a simplified ship collision decoupling method named the CAM method. The CAM method involves considering the influence of surrounding fluid on a collision by attaching a certain mass to the collision structure. Due to its simplicity, the CAM method has attracted great interest in ocean engineering and is widely used in ship collision analysis. The slicing method and an empirical formula can be used to estimate the CAM of a structure involved in a collision.

Minorsky [28] proposed a simple empirical formula for additional mass during lateral drift:

$$M_{yy} = 0.4m \tag{1}$$

where M_{yy} is the additional mass and m is the quality of the ship.

The CAM of the ship is not a fixed value during horizontal drift. The longer is the collision time, the greater is the added mass. The CAM variation range can be shown as follows:

$$M_{yy} = (0.4 \sim 1.3)m \tag{2}$$

When the ship is forward and backward, its additional mass is expressed as

$$X_H(t) = -a \cdot M_{xx} \tag{3}$$

where $X_H(t)$ is the hydrodynamic force acting on the ship, a is the acceleration of the forward and backward movement of the ship, and M_{xx} is much smaller than the ship's mass m. The following equation can be used to estimate M_{xx}:

$$M_{xx} = (0.02 \sim 0.07)m \tag{4}$$

Motora et al. [29] studied the effectiveness of Minorsky's assumption of CAM by using a series of test models and concluded that the aforementioned assumption is only valid for short-duration collisions. For collisions of a longer duration, the value of additional mass increases to even higher than the value of the ship's mass. In addition, the CAM method does not consider the relative motion between water and a structure or the wetted surfaces of the two objects during a collision. In this study, the CAM method was used only to consider the hydrodynamic added mass of a ship; the CAM coefficient of the ship was set to 0.05 for simplicity.

3. Collision simulation

Collision simulation is a key step for establishing the safety of TLPWTs in service. To illustrate the influence of a collision on TLPWTs, in this study, overall structural responses, the internal force of tension legs, and cabin responses were analyzed. The overall collision simulation was performed using LS-DYNA. Except for collision force, our study did not involve consideration of other external environmental factors such as wind and waves, because these have a markedly lower impact than does collision force; this approach is consistent with those of other authors [30]. The results revealed that although under certain circumstances waves have an adverse effect on a collision, collision force and depth were almost the same as those under wave-free conditions.

3.1. Numerical model

In this study, a parked 5-MW TLPWT was employed as an example, as depicted in Fig. 1. This TLPWT was studied previously [31]; and it was called the National Renewable Energy Laboratory offshore 5-MW baseline wind turbine. Four tension legs groups, each comprising two tension legs, support the TLPWT. The main parameters of the TLPWT model are listed in Table 1.

As illustrated in Fig. 1, the origin of the coordinates is at the bottom of the platform's central column. The x- and y-axes are parallel to the axis of the pontoon, and the z-axis is vertical to it. The remaining parameters (e.g., speed, angle) are based on the aforementioned coordinates without other special instructions.

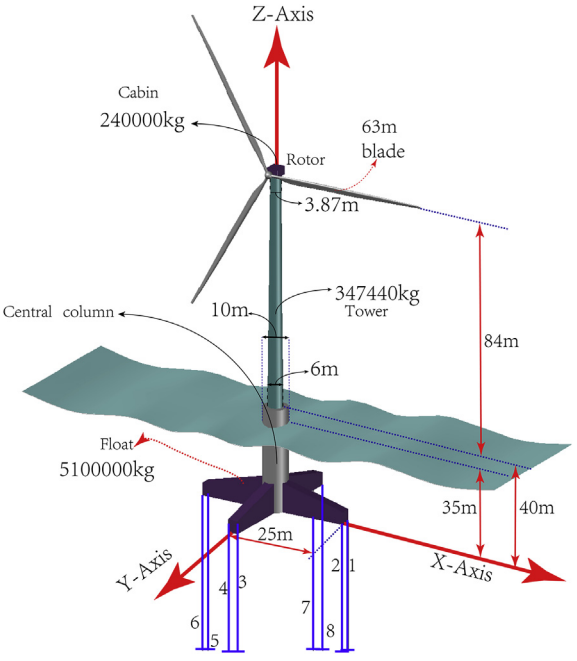

Fig. 1. TLPWT.

Table 1. TLP parameters [31].

Items	Value (Unit)
Column outer wall thickness	20 (mm)
Platform weight	5.1×10^6 (kg)
Inner height of the pontoon	11(m)
Float outer wall thickness	20 (mm)
Rib thickness	20 (mm)
Platform displacement	5.98×10^6 (kg)
Outside height of the pontoon	5(m)

$$p = \begin{cases} \dfrac{\rho_0 C^2 \mu \left[1 + \left(1 - \dfrac{\gamma_0}{2}\right)\mu - \dfrac{a}{2}\mu^2\right]}{\left[1 - (S_1 - 1)\mu - S_2\dfrac{\mu^2}{\mu+1} - S_3\dfrac{\mu^3}{(\mu+1)^2}\right]^2} + (\gamma_0 + \alpha\mu)E_i & (compressed\ material) \\ \rho_0 C^2 \mu + (\gamma_0 + \alpha\mu)E_i & (expanded\ material) \end{cases} \quad (6)$$

The material chosen for the TLPWT numerical model was steel, and material was considered nonlinear due to its large plastic deformation during collision. In this study, a plastic dynamic model was adopted that can consider strain hardening and maximum plastic failure strain [32]. Once an element reaches the maximum plastic failure strain, the element ruptures, the stress is equal to zero, and external load can no longer be borne.

The plastic properties of marine low-carbon steel are highly sensitive to strain rate. The yield stress and tensile strength limits of such steel increased with strain rate, and thus, the influence of strain rate should be introduced in a material model. In this study, the Cowper−Symonds constitutive equation [33] was used to consider strain rates, and the numerical results were consistent with experimental data [34]. The formula for strain rate is as follows:

$$\sigma_y = \left[1 + \left\{\frac{\dot{\varepsilon}}{D}\right\}^{\frac{1}{P}}\right]\left(\sigma_0 + \beta E_p \varepsilon_p^{eff}\right) \quad (5)$$

where σ_0 is the initial yield stress, $\dot{\varepsilon}$ is the effective plastic strain rate, E_p is the plastic hardening modulus given by $E_p = E_h E/(E - E_h)$, ε_p^{eff} is the effective plastic strain, β is the hardening parameter, E_h is the tangent modulus, E is the elastic modulus, D is 40.4, and P is 5. The material parameters are detailed in Table 2.

When the FSI was used in this study, a null material model was to simulate water and air. The pressure−volume relationship of the null material model is defined using the Gruneisen state equation [26]. The pressure for compressed and expanded materials in the null material model are calculated as follows:

$$\mu = \frac{\rho}{\rho_0} - 1 \quad (7)$$

where E_i is the internal energy per initial volume, ρ_0 and ρ are initial density and current density, respectively, and C is the intercept of the $u_s - u_p$ curve (u_s is the velocity of the shock wave, u_p is the velocity of the medium particle, and the characteristic curve of the material in the $u_s - u_p$ coordinate system is called the $u_s - u_p$ characteristic curve). S_1, S_2, and S_3 are the coefficients of the $u_s - u_p$ curve, γ_0 is the Gruneisen gamma, and a is the first order volume correction to γ_0. Constants C, S_1, S_2, S_3, γ_0, and a are user-defined input parameters that can be obtained directly from experiments.

The structure studied in this paper had eight tension legs. Their material parameters are listed in Table 4.

The initial pretension of all tension legs was set to 1.075×10^6 N. The internal force was affected by buoyancy, pretension, and gravity.

3.2. Finite element model

For the finite element model (FEM), a conventional supply ship with 5000-Mg mass [35] crashed

Table 2. Plastic material parameters.

Material properties	Value (unit)
Density	7800 (kg/m^3)
Young's modulus (E)	2.10×10^{11}(Pa)
Passion ratio	0.3
Initial yield Stress (σ_0)	2.35×10^8(Pa)
Tangent modulus (E_h)	1.18×10^9(Pa)
Hardening rate (β)	0
Failure strain	0.34

Table 3. Water and air material parameters (in null material model).

Material properties	Water	Air
Density (kg/m^3)	1025	1.226
C (m/s)	1650	344
S1	1.92	0
S2	−0.096	0
S3	0	0
γ_0	0.35	1.40

Table 4. Geometrical and material parameters of tension legs.

Material	Section diameter(m)	length(m)	Axial stiffness(N)	Dry weight (kg/m)	Break strength(N)
Steel cable	0.10	200	9.891×10^8	55.46	1.0×10^7

into the wind turbine along the negative x-axis at 3 m/s. The geometric model of the ship is presented in Fig. 2. Because the bulb bow has sufficient stiffness and the collision response of the TLP was the principal concern in this study, only the bow model was built to simulate the whole ship's behavior. The ship's bow had the same mass, collision speed, and inertia moment as the whole ship did. The bow's FEM is depicted in Fig. 2(b).

To reduce the number of elements and enhance the calculation efficiency, some minor ribs were neglected during construction of the FEM, and the wind turbine was simplified as a mass. Shell 163 elements were used to simulate the shell and ribs at the column and pontoon depicted in Fig. 1. Link 167 elements were to simulate the tension legs. The simplified FEM, which refines the elements at the areas where collision occurs, is illustrated in Fig. 3.

Additionally, in the FSI analysis model, the overall area of the fluid was 200 m × 120 m × 80 m (length × width × height). The air and water in the fluid were simulated using Solid 164 elements. All material parameters for the FEM are shown in Tables 2–4.

3.3. Contact and boundary conditions

To avoid initial penetration, the ship was configured to maintain an initial distance of 0.9 m from the TLPWT, as illustrated in Fig. 3. During collision, the master and slave contact interfaces were defined as the ship bow and the refined elements in the TLP, respectively. The coefficients of dynamic friction and static friction were both set to 0.2 during contact.

The TLPWT was constrained by its tension legs, which had fixed bottoms. A nonreflective boundary constraint was applied around the fluid due to the flow field being infinite.

4. Results

Based on the aforementioned theory and numerical model, this paper details the simulation of collisions between a ship and TLPWT.

4.1. Velocity and force during collision

The velocity and the collision force are displayed in Fig. 4.

Figure 4 shows that the collision force began to appear at 0.3 s and reached a maximum at 0.645 s. It began dropping rapidly thereafter until it reached zero at 1.025 s; hence, the TLP was separated from the ship at that time. From 0.3 to 0.645 s, the ship velocity decreased almost linearly, but the TLP velocity increased almost linearly, thus explaining the eventual separation. After 1.560 s, the collision force reoccurred and increased to 7.14×10^6 N. It then began to decrease, reaching zero again at 2.205 s. This indicates that the second collision occurred between 1.560 and 2.205 s. From 1.025 to 1.560 s, the ship velocity was always higher than the TLP velocity; this explains the second collision. During the second collision, the ship velocity decreased gradually and was less than the TLP velocity at 1.950 s. At 2.205 s, the ship separated from the TLP again, and ship speed tended toward a certain nonzero value when water resistance was ignored. Under the influence of interactions between the tension legs

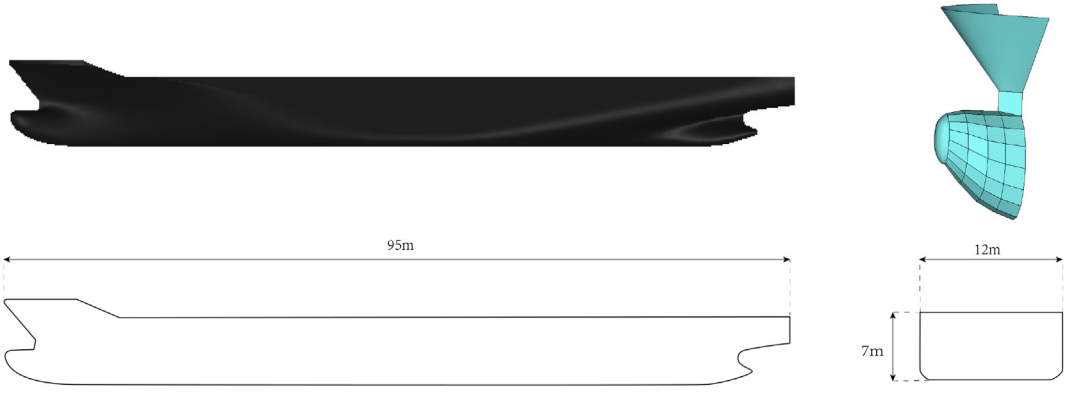

Fig. 2. Ship geometry model & the finite element model of the bow.

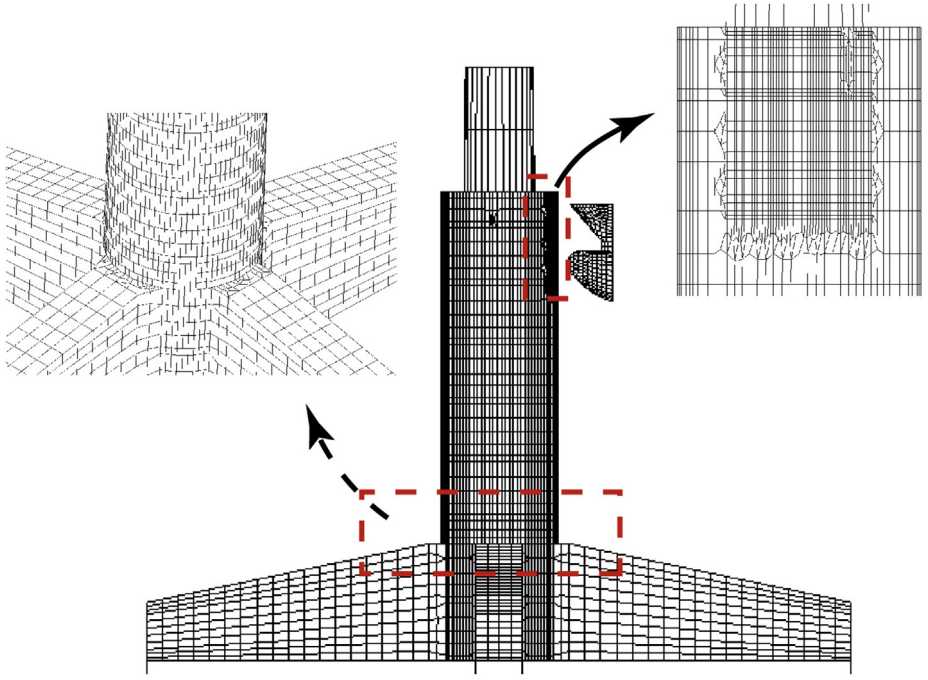

Fig. 3. Finite element model.

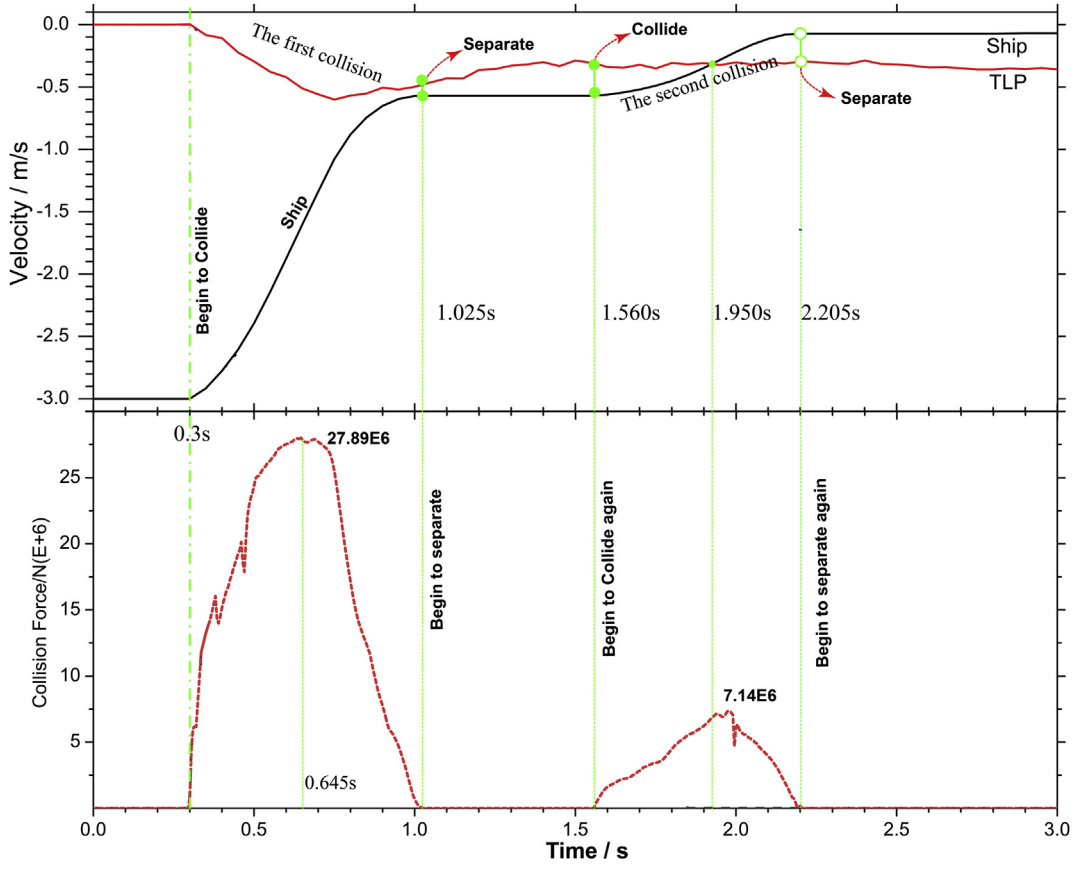

Fig. 4. Velocity and collision force curves.

and water, the TLP slowly vibrated and moved. Its velocity tended toward zero because of the effect of water resistance. The maximal collision force of 27.89×10^{6} N appeared during the first collision.

4.2. System energy analysis

The energy conversion between the ship and TLPWT during collision is the key factor in assessing the rationality of the simulation results. The energy conversion results are displayed in Fig. 5.

Figure 5 demonstrates that the total energy of the system and initial kinetic energy of the ship are both 23.62 MJ. Energy conversion mainly occurred during the first collision (i.e., from 0.3 to 1.025 s) when the kinetic energy of the ship was primarily converted into system internal energy, platform kinetic energy, water kinetic energy, and ship residual kinetic energy. The system's hourglass energy could account for less than 1.7% of the total energy, and the energy conversion was generally consistent with the law of conversion of energy, which indicates that the collision calculation results were acceptable. Throughout the collision process, the kinetic energy and the internal energy transformed into each other, and the system internal energy accounted for more than 80% of the total energy. It is understood that during collision, the initial energy is mainly be converted into a system's internal energy.

4.3. Structural damage analysis

The damage deformation of the structure can be reflected by plastic strain. Figure 6 shows the plastic strain cloud diagram at the collision zone of the TLPWT at different times.

Figure 6 suggests that plastic failure mainly occurred at the collision area involving the upper part of the bulb bow and the bow parts. The deformed shapes of the two impact zones are related to the shape of the bow structure. At 0.45 s, the strain was smaller than the material failure strain of 0.34, which indicates that failure did not occur before this time point. As the impact force increased rapidly during the collision, the unit plastic strain reached the failure value of 0.34 after 0.45 s. According to the calculated results from LS-DYNA, the shell element 20163 failed at 0.486 s and until the end of the entire collision process, and no other element in the entire structure reached the failure strain value of 0.34. The area of the plastic deformation cloud map suggests that the plastic deformation gradually increased with the progress of the collision (i.e., from 0.3 to 1.025 s), and the failure area was not the largest when the impact force was at its maximum, at 0.645 s. Instead, after the peak of the impact force, the plastic failure area continued to expand until the separation of the ship and TLP.

In addition to plastic deformation at the collision area, Fig. 7 presents the equivalent stress cloud of the TLPWT at 0.65 s when the collision force was almost at its maximum.

Figure 7 indicates that the maximum stress in the collision zone was 586.5 MPa, which is approximately 2.5 times the material static yield stress (235 MPa). Notably, the stress at the joint between the pontoon and the central column also exceeded 235 MPa. During the collision, the stress was concentrated in the collision zone and the connection area between the central column and the pontoon and tower. These areas should be protected at the platform design stage.

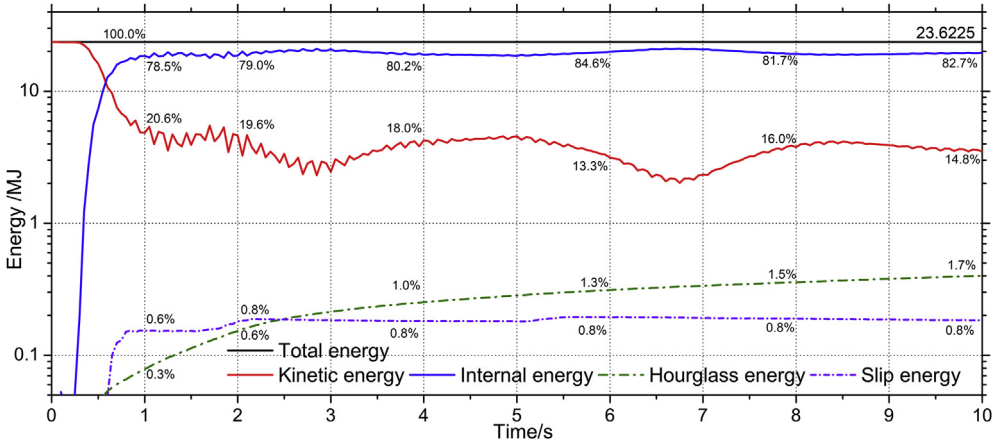

Fig. 5. System energy conversion curves.

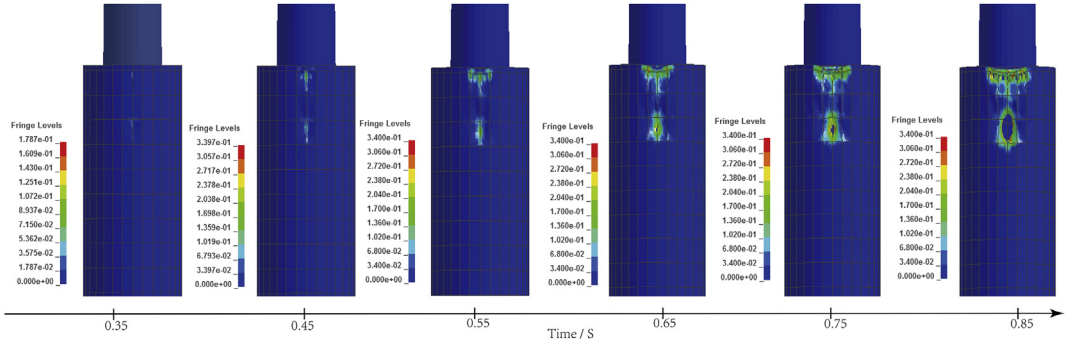

Fig. 6. Plastic strain cloud diagram at the collision zone (3 m/s).

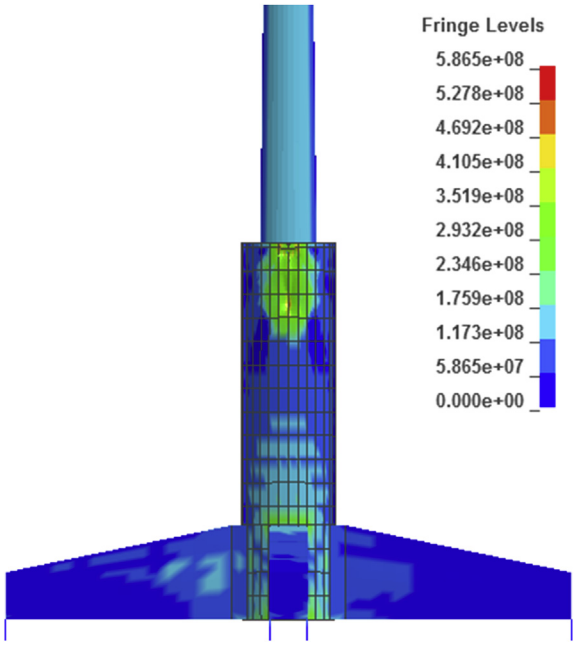

Fig. 7. Equivalent stress cloud map (v = 3 m/s, t = 0.65 s).

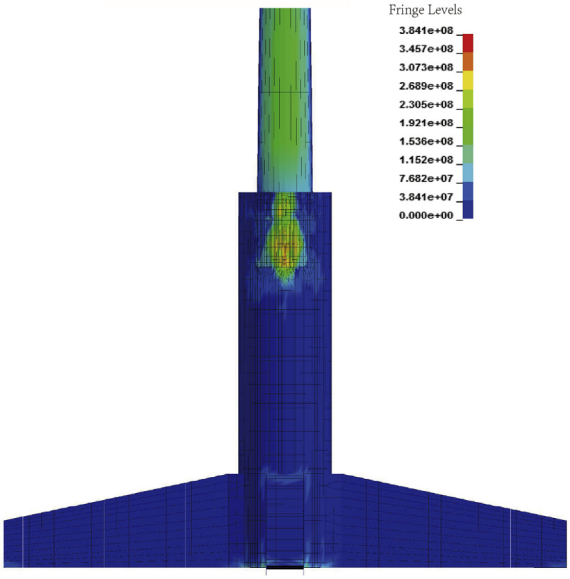

Fig. 9. Equivalent stress cloud map (v = 2 m/s, t = 0.75 s).

The plastic strain and equivalent stress cloud diagrams of the TLPWT when the initial speed of ship was reduced to 2 m/s are depicted in Figs. 8 and 9, respectively.

Figure 8 indicates that the strain value was always smaller than the material failure strain value of 0.34. The maximal strain value was 0.2963. Figure 9 shows that the maximum stress in the collision zone was 384.1 MPa, which was lower than 586.5 MPa at 2 m/s. The plastic strain and equivalent stress cloud diagrams of the TLPWT when the initial speed of ship is increased to 5 m/s are shown in Figs. 10 and 11, respectively.

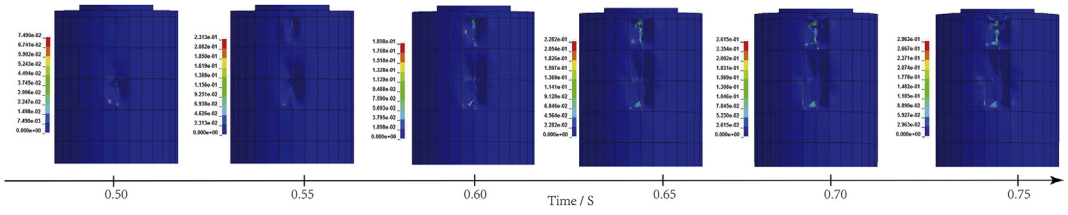

Fig. 8. Strain cloud diagram of the collision area (2 m/s).

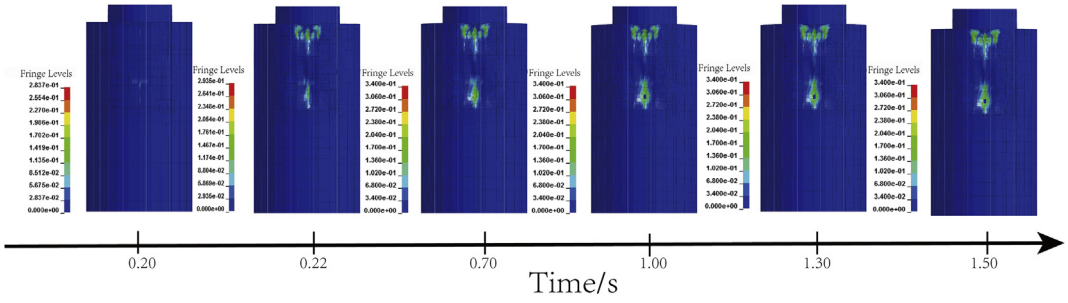

Fig. 10. Strain cloud diagram of the collision area (5 m/s).

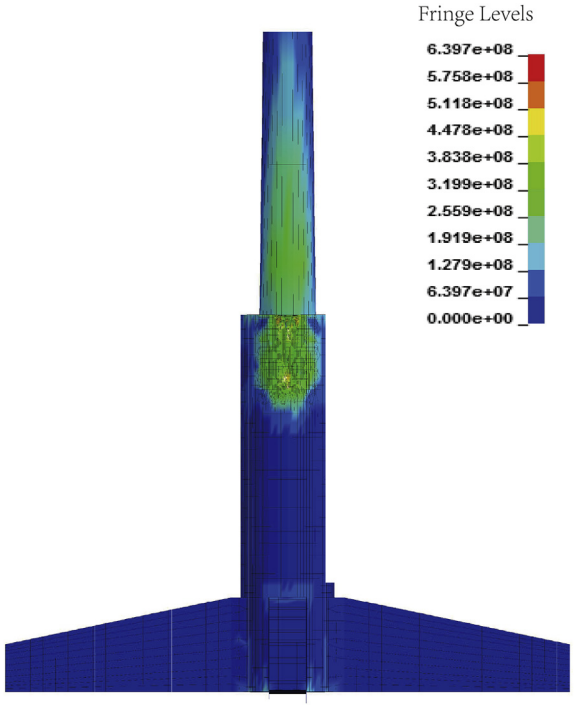

Fig. 11. Equivalent stress cloud map ($v = 5$ m/s, $t = 0.4$ s).

Figure 10 shows that the unit plastic strain reached the failure value of 0.34 after 0.22 s. The collision damage at 5 m/s appeared markedly earlier than did that at 3 m/s. Figure 11 reveals that the maximum stress value in the collision zone was 639.7 MPa, which is markedly higher than the values at 2 and 3 m/s. These results suggest that the higher is the speed of the ship, the greater is the collision damage to the platform; thus, reducing ship speed is an effective approach for reducing collision damage.

4.4. Internal force of tension legs

Tension legs are key components of a stable TLPWT; if tension legs fracture, they fail to support the TLPWT. Thus, the internal force of tension legs during a collision is also of critical interest. The response of tension legs during a collision is characterized in Fig. 12.

Figure 12 shows that the axial force magnitudes and curve trends of legs 1 and 2, 3 and 8, 4 and 7, and 5 and 6 were essentially the same because these tension leg pairs were each symmetrical with one another. The tension legs located on the positive half of the x-axis

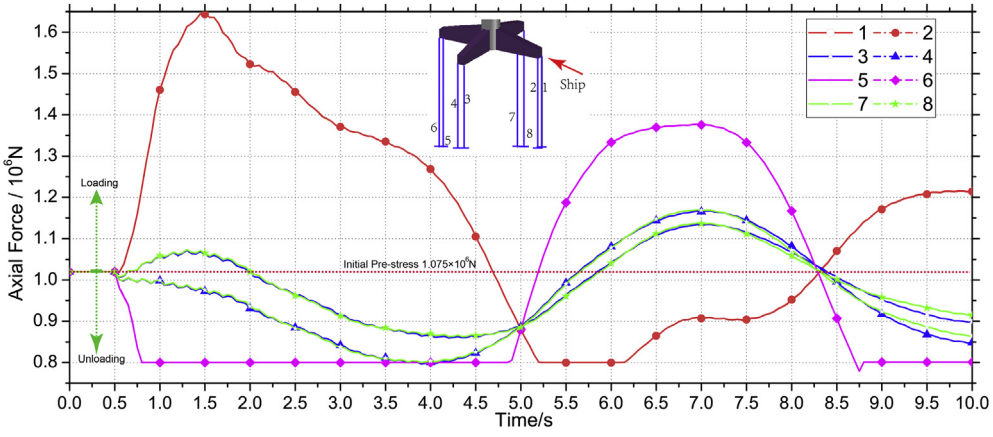

Fig. 12. Axial force of tension legs.

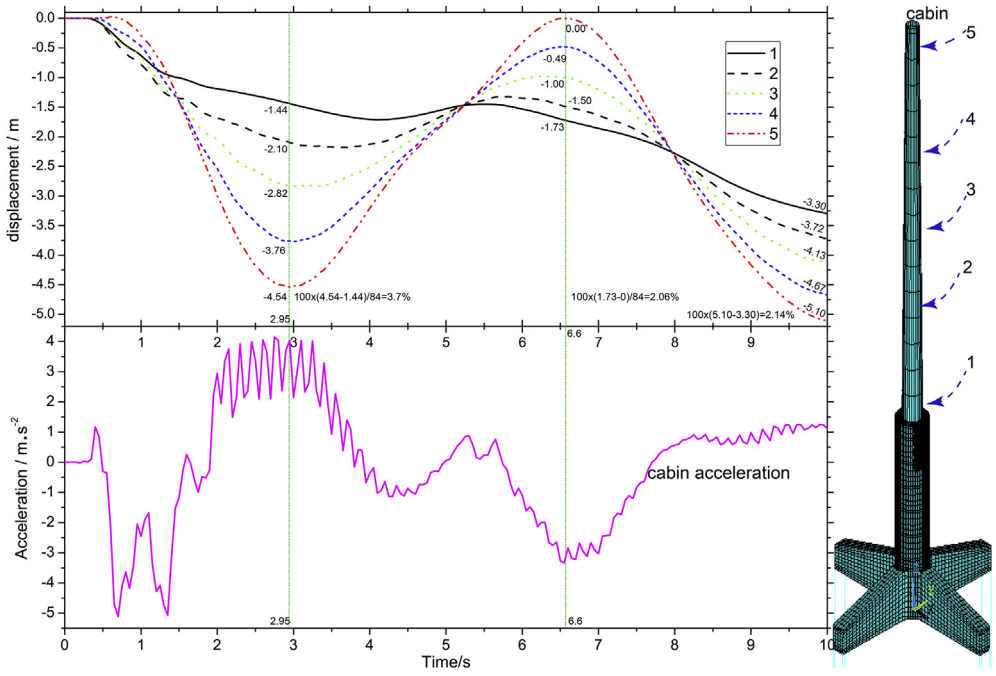

Fig. 13. Displacement of the tower and cabin acceleration in the x direction.

(tension legs 1, 2, 3 and 8) were first loaded and then unloaded. The internal force trend of tension legs on the negative half of the x-axis (tension legs 4, 5, 6, and 7) was exactly opposite. This was caused by the pitch of the TLP around the y-axis after collision. In addition, the axial force variation of the tension legs near the y-axis coordinate was small, whereas the divergence of tension legs 1 and 2 away from the y-axis was greatest among that of all the tension legs pairs; their axial force increased from 1.075×10^6 N to 1.645×10^6 N. The axial force of each tension key was concentrated at 0.88×10^6 N at 5 s; this value is lower than the initial pretension value of 1.07×10^6 N, indicating that the collision caused the rigid displacement of the TLPWT in the negative direction of the z-axis at this time point. After 5 s, the tension legs tightened again under the influence of buoyancy, and their axial forces gradually returned to their pretension value. None of the tension legs exhibited the relaxation phenomenon. Hence, enhancing the initial prestress of tension legs an effective method of avoiding tension leg relaxation. Figure 12 also reveals that the internal force was always less than the break strength (i.e., 1.0×10^7 N); thus, the tension legs were not at risk of breakage.

4.5. Tower top cabin response analysis

The nacelle is a key component for normal operation of wind turbines; thus, a response analysis of a cabin during a collision is essential. Figure 13 lists the displacement response of the tower and the acceleration of the cabin in the x direction at different times.

All five nodes had displacement on the negative x-axis, indicating that the TLPWT exhibited rigid body displacement after the collision. The displacement of the five nodes at different stages suggested a waveform growth, indicating that the tower was pitching back and forth and coupled with rigid displacement. The pitch amplitude reached the first peak of −4.52 m (the displacement difference between the tower bottom and its top node) at approximately 3 s, and the second peak of 0 m occurred at 6.6 s. The pitch degrees were 3.7%, 2.06%, and 2.14% of the height of the tower (124m) at 2.95, 6.6 and 10.0 s, respectively. The pitch amplitude decreased over time due to the resistance of water. The acceleration of the cabin in the x direction increased rapidly after a collision, and its direction was opposite to the collision force; hence, cabin inertial force (rather than collision force) caused the acceleration of the cabin at this stage. The acceleration reached a maximum value (-5.11 m/s^2) at 0.7 s and then gradually decreased. In general, except for the first peak, the acceleration of the cabin reached the local largest value when the tower pitch amplitude was at its maximum.

5. Conclusion

In this study, a collision between a ship and a TLPWT was simulated. The fluid around the TLPWT and the ship was analyzed using FSI and

CAM methods, respectively. Several conclusions can be drawn from the collision simulation results.

First, the fluid around the collision objects is a key factor during a collision. Although the FSI method is more time-consuming and occupies more computational resources than the CAM method, using the FSI method to study the effects of water conditions on research objects (e.g., TLPWT) is recommended. In this study, the ship was the only object that produced collision force; thus, the fluid around the ship was considered using the CAM method. Second, the stress was concentrated in the collision zone and the connection area between the central column and the pontoon and the tower. Hence, limiting ship speed is an effective approach for preventing collision damage. Third, tension legs are key components of TLPWTs. Enhancing the initial prestress of tension legs helps to avoid tension leg relaxation.

Finally, the tower of the wind turbine tended to pitch back and forth, coupling with a rigid displacement after collision, and the acceleration of the cabin reached the local largest value when the tower pitch amplitude reached its local maximum.

Declaration of competing interest

The authors declare that they have no known competing financial interests or personal relationships that could have appeared to influence the work reported in this paper.

Acknowledgments

This work has been supported by State Key Laboratory of Ocean Engineering (Shanghai Jiao Tong University) (No.1709).

References

[1] Kausche M, Adam F, Dahlhaus F, Großmann J. Floating offshore wind - economic and ecological challenges of a TLP solution. J Renewable Energy 2018;126:270−80.
[2] Arany L, Bhattacharya S, Macdonald J, Hogan SJ. Design of monopiles for offshore wind turbines in 10 steps. J Soil Dynamics and Earthquake Engineering 2017;92:126−52.
[3] Duan F, Hu ZQ, Niedzwecki JM. Model test investigation of a spar floating wind turbine. J Marine Structures 2016;49:76−96.
[4] Kvittem MI, Moan T. Time domain analysis procedures for fatigue assessment of a semi-submersible wind turbine. J Marine Structures 2015;40:38−59.
[5] Oguz E, Glelland D, Day AH, Incecik A, Lopez JA, Sánchez G, et al. Experimental and numerical analysis of a TLP floating offshore wind turbine. J Ocean Engineering 2018;147:591−605.
[6] Bachynski EE, Moan T. Design considerations for tension leg platform wind turbines. J Marine Structures 2012;29(1):89−114.
[7] Nematbakhsh A, Olinger DJ. A nonlinear computational model of floating wind turbines. J Fluids Engineering 2013; 135(12):1−13.
[8] Martin HR, Kimball RW, Viselli AM, Goupee AJ. Methodology for wind/wave basin testing of floating offshore wind turbines. J Offshore Mechanics and Arctic Engineering 2014;136(2).
[9] Goupee AJ, Koo BJ, Kimbal RW, Lambrakos KF, Dagher HJ. Experimental comparison of three floating wind turbine concepts. J Offshore Mechanics and Arctic Engineering 2013; 136:901−9.
[10] Rio Prabowo A, Myung Bae D, Min Sohn J, Fauzan Zakki A, Cao B, Hyung Cho J. Effects of the rebounding of a striking ship on structural crashworthiness during ship-ship collision. J Thin-Walled Structures 2017;115:225−39.
[11] Sha YY, Amdahl J, Dorunm C. Dynamic responses of a floating bridge subjected to ship collision load on bridge girders. J Procedia Engineering 2017;199:2506−13.
[12] Travanca J, Hao H. Energy dissipation in high-energy ship-offshore jacket platform collisions. J Marine Structures 2015; 40:1−37.
[13] Minorsky VU. An analysis of ship collision to protection of nuclear powered plan. C Journal of Ship Rsearch 1959;27(1):1−4.
[14] Paik JK. Cuting of a longitudinally stiffened plate by a wedge. J Journal of Ship Research 1994;38(4):340−8.
[15] Prabowo AR, Baek SJ, Byeon JN, Bae DM, Cho JH, Sohn JM. Investigation on the structural damage of a double-hull ship, Part I−ship collision. J Procedia Structural Integrity 2017;5:943−50.
[16] Moulas D, Shafiee M, Mehmanparast A. Damage analysis of ship collisions with offshore wind turbine foundations. J Ocean Engineering 2017;143:149−62.
[17] Gjerde P, Parsons SJ, lgbenabor SC. Assessment of jack-up boat impact analysis methodology. J Marine Structures 1999; 12(4):371−401.
[18] Ren NX, Ou JP. Dynamic numerical simulation for ship-OWT collision. In: 2009 8th International Conference on reliability, Maintainability and safety; 2009. p. 1003−7.
[19] Hamann T, Pichler T, Grabe J. Numerical simulation of ship collision with gravity base foundations of offshore wind turbines. In: C Proceedings the 32nd International Conference on ocean, offshore and arctic engineering. France: Nantes; 2013.
[20] Hao E, Liu C. Evaluation and comparison of anti-impact performance to offshore wind turbine foundations: monopile, tripod, and jacket. J Ocean Engineering 2017;130:218−27.
[21] Bela A, Sourne LH, Buldgen L, Rigo P. Ship collision analysis on offshore wind turbine monopile foundations. J Marine Structures 2017;51:220−41.
[22] Mo RJ, Li M, Kang HG. Transient behaviour of grouted connections of offshore wind turbines subject to ship impact. J Applied Ocean Research 2018;76:159−73.
[23] Ren NX, Ou JP. A crashworthy device against ship-OWT collision and its protection effects on the tower of offshore wind farms. J China Ocean Engineering 2009;23(4): 594−602.
[24] Song M, Ma J, Huang Y. Fluid-structure interaction analysis of ship-ship collisions. J Marine Structures 2017;55:121−36.
[25] Song M, Kim E, Amdahl A, Ma J, Huang Y. A comparative analysis of the fluid-structure interaction method and the constant added mass method for ice structure collisions. J Marine Structures 2016;49:58−75.
[26] LSTC. LS-DYNA User's manual, version 971 R5. USA: Livermore Soft Technology Corp; 2011.
[27] Minorsky VU. An analysis of ship collision with reference to protection of nuclear powered plants. J Ship Res 1959;3(2): 1−4.
[28] Minorsky VU. An analysis of ship collision to protection of nuclear powered plant. C Journal of Ship Rsearch 1959;27(1):1−4.
[29] Motora S, Fujino M, Sugiura M. Equivalent added mass of ships in the collisions. J The Japan Society of Naval Architects and Ocean Engineers 1971;7:128−38.
[30] Song M, Ma J, Huang Y. Study of effect of wave on ship collision. J Journal of Dalian University of Technology 2014;4: 433−7 [In Chinese)].

[31] Jonkman J, Butterfield S, Musial W, Scott G. Definition of a 5-MW reference wind turbine for offshore system development.
[32] Zhang ML, Chen Z, Zhao S. The determination of element failure strain with the element removal method. J Chinese Journal of Ship Research 2013;2:46−52+64 [In Chinese)].
[33] Jones N. Structural impact[M]. New York: Cambridge University Press; 1997.
[34] Zhi XD, Zhang R, Lin L, Fan F. Dynamic constitutive model of Q235B steel and its application in LS-DYNA. J Explosion and Shock Waves 2018;38(3):596−602 [In Chinese)].
[35] Gu JY, Deng BL, Yang LC, Guo XT. Method of fast evaluation of ship-platform collision dissipated energy based on analytical method. J Journal of ship mechanics 2017;z1: 363−74 [In Chinese].